Renewable Energy 146 (2020) 371–383

Contents lists available at ScienceDirect

Renewable Energy

journal homepage: www.elsevier.com/locate/renene

Predicting the stochastic aerodynamic loads on blades of two yawed downwind hawts in uncontrolled conditions using a bem algorithm

Moutaz Elgammi [a, *], Tonio Sant [b], Moftah Alshaikh [a]

[a] Department of Mechanical Engineering, University of Omar Al-Mukhtar, Derna, Libya
[b] Department of Mechanical Engineering, University of Malta, Msida MSD, 2080, Malta

ARTICLE INFO

Article history:
Received 3 August 2018
Received in revised form
6 March 2019
Accepted 20 June 2019
Available online 27 June 2019

Keywords:
Cycle-to-cycle aerodynamic loads
BEM model
Yawed rotor
Turbulent wind
Dynamic stall
Stall delay

ABSTRACT

Accurate predictions of the cycle-to-cycle variations in aerodynamic loads on wind turbine blades are important for estimating the life cycle costs of new wind power plants. Physical modelling of wind turbine systems is usually based on the average values of the aerodynamic parameters in the design process which would eliminate some important physical phenomena associated with the unsteady flows over the rotating blades. This paper presents a new algorithm implemented in a Blade Element Momentum (BEM) model to predict the cycle-to-cycle variations in the aerodynamic loads over multiple rotor rotations (cycles) for yawed rotors operating in natural flow conditions. In this approach, simulation theory developed by the Pacific Northwest Laboratories (PNL) is used to generate input turbulent wind speed time series on the whole rotor disc of two three-bladed downwind horizontal axis wind turbine (NREL Phase II and III) rotors. The unsteady influences of the dynamic stall kinematics and tower shadow are also considered in the current algorithm along with the phenomenon of stall delay. Predictions from the unsteady BEM model are compared to measured results and conclusions are drawn about the ability of the model to accurately simulate blade response to turbulence.

1. Introduction

Prediction of the extreme load responses and lifetime of a wind turbine structure is challenging due to the 3D complex unsteady aerodynamic flow environment. The major difficulties in measuring and predicting the performance and structural loads are due to several unsteady sources such as variations in wind speed, atmospheric turbulence, wind shear, tower shadow effects and yawed flow. Instabilities in the vortical wake downstream of the wind turbine may also lead to unsteady flow conditions over the rotating blades. Combining the elastic deformation of the blade with these unsteady loads can lead to significant cycle-to-cycle variation in the aerodynamic loads, instabilities and fatigue. Beside the unsteady effects, the flow around a rotating blade is further subjected to the stall delay phenomenon. These aspects have been discussed in Refs. [1–6].

Measurements of the cycle-to-cycle variations in blade loading under dynamic stall conditions showed that the fluctuations in the aerodynamic loads and flow reattachment process vary significantly from one cycle to another. It was also shown that the cycle-to-cycle variations in the aerodynamic loads are small in the attached flow regimes, while they are significant in the deep stall and reattachment flow regimes [7]. Such observations were already confirmed in the experimental work of Mulleners et al. [8]. Li *el al.* [9] conducted an experimental investigation on the effect of different turbulence intensities on the aerofoil performance of a HAWT model in static stall. It was shown that the turbulence intensity has no dramatic impact on the linear lift force coefficient. Blade surface pressure measurements conducted on the NREL Phase VI rotor in yawed conditions also showed that dynamic stall causes the wind turbine blades to experience significant cycle-to-cycle variations in aerodynamic loading. These effects were observed even though the rotor was subjected to a fixed speed and a uniform and steady wind flow [10,11].

Various experimental studies have been performed on full-scale HAWTs over the past few decades by operation in atmospheric flow environment and tests in wind tunnels. One of the most well-known measurements in natural conditions was conducted by the National Renewable Energy Laboratory's (NREL) way back in 1987. Two tests were performed: (i) Phase I and II: Blade without

* Corresponding author.
E-mail addresses: moutaz.elgammi@omu.edu.ly (M. Elgammi), tonio.sant@um.edu.mt (T. Sant), moftah.alshaikh@omu.edu.ly (M. Alshaikh).

https://doi.org/10.1016/j.renene.2019.06.114
0960-1481/

twist and taper, and (ii) Phase III and IV: Blade without taper but with twist. The use of the test facilities and experimental results has been documented by Schepers [12], Butterfield *el al.* [13,14], Acker and Hand [15] and Fingersh et al. [16]. The measurement data of Phase I & II were analysed by Butterfield *el al* [13,14]. The results were compared to wind tunnel test data obtained under controlled conditions. It was found that stall delay is prominent in all operating conditions. Dynamic stall phenomenon and aerodynamic load hysteresis loops were evident even for small yaw angles. The cycle to cycle variations in various aerodynamic parameters are significant at the inboard sections of the blade and reduce gradually when moving towards the blade the tip sections. Constant chord and zero twist were also found to reduce the impact of blade geometry on stalled flow. Acker and Hand [15] analysed the measured data of the NREL wind turbine Phase IV rotor. The degree of penetration of the dynamic stall event for this wind turbine with twisted blades was dramatically lower than that observed on the untwisted blades of the NREL wind turbine Phase II rotor. These studies are helpful to understand the influences of the twisted, untwisted, and the different pitch settings on both stall delay and dynamic stall phenomena. Other measurements in the open field environment were also performed by: the Netherlands Energy Research Foundation (ECN), Delft University of Technology (DUT), Imperial College and Rutherford Appleton Laboratory (IC/RAL), and Risø National Laboratory (Risø). These measurements have been performed under the IEA R&D wind program: IEA Annex XIV (from 1991 to 1997) "Field Rotor Aerodynamics" [17] and IEA Annex XVIII (from 1997 to 2001) "Enhanced Field Rotor Aerodynamics Database" [18]. Further details can be found in Schepers and van Rooij [19]. These measurements formed a basis for understanding wind turbine aerodynamic behaviour, improving the design of wind turbine systems, and enhancing the analysis of wind turbine aerodynamics under different operating conditions.

Accurate aerodynamic measurements in natural conditions are difficult and time consuming due to the stochastic nature of the wind. Under these conditions, the high level of uncertainty resulting from the non-stationary, inhomogeneous, and uncontrolled wind conditions is also hard to be predicted by potential flow theories [20]. There are various theories exist to model the rotor performance of a wind turbine such as Blade Element Moment (BEM) method, Free-Wake Vortex (FWV) methods, and Computational Fluid Dynamics (CFD) method. These methods are reviewed in Refs. [1,20–22]. The Blade Element Momentum (BEM) theory is considered to be the most straight forward model due to its low computational cost and its reasonable accuracy. FWV and CFD methods are more physically comprehensive than BEM, but are more complex and computational costly methods. Therefore, these are not the desired methods for wind turbine design processes where many routine computations have to be carried out [20].

Although turbulent wind effects on the structures of wind turbines are recognized, the current numerical BEM-based models developed for wind turbine design are not yet capable to model the turbulence-induced blade loads with a high degree of reliability. These were clarified in a blind comparison study conducted by NREL [11] and from the Mexnext-I project [23]. This is also evident from the blind test comparison under different turbulent inflow conditions that was held in Trondheim in 2015 [24]. The deviation and discrepancies in the predicted results of various simulation tools, including BEM, were evident indicating that further improvement in the basic aerodynamics algorithms is required to develop more rigorous models crucial for more reliable predictions of wind turbine performance, wind turbines design process, and fatigue loads.

The present work was conducted to provide a modified Blade Element Momentum (BEM) based code to estimate the unsteady aerodynamic loads on a downwind horizontal axis wind turbine blades taking into account the combined influences of turbulent wind, tower shadow, yawed flow, dynamic stall, and stall delay under natural flow conditions. This paper will first describe the two reference wind turbines modelled in this analysis and the selected measurements used for the validation of the modified BEM code. This is followed by an overview of the modifications implemented to the classical BEM approach. The developed model is next validated against measurements conducted on two three-bladed downwind HAWT (NREL Phase II and III) rotors. The newly proposed BEM algorithm provides new insight to improve modelling of blade loads under turbulent flow conditions by addressing the following two aspects:

- A rotating wind turbine blade is exposed to turbulence whose characteristics are different from the turbulence measured using a stationary anemometer [25]. In this paper, the influence of wind fluctuations on a rotating blade is modelled using a theoretical simulation method: the Pacific Northwest Laboratories (PNL) Simulation theory [26] that is implemented in a new BEM algorithm. Unlike the Kamial and von Karman models which simulate turbulence at a fixed point, the PNL model directly caters for the rotational effect and thus its results are more representative of the turbulence experienced by a wind turbine blade. Therefore, this tool is expected to be vital for design purposes to evaluate the amount of turbulence energy distributed with the frequency of fluctuations on a rotating blade rather than that used traditionally for a stationary point only.
- Experiments showed that significant cycle-to-cycle variations in aerodynamic loading under the combined influence of stall delay and dynamic stall phenomena are evident, not only in the free environmental conditions but also under a fixed speed and a uniform and steady wind flow [27]. Therefore, modelling the influence of the rotor self-induced aerodynamic load fluctuations on the variations of various unsteady aerodynamic parameters in yawed flows using a fast and more reliable BEM algorithm is of great importance to have lighter turbine blades and improved wind turbine design systems.

2. Specifications of the reference wind turbines and test configurations

The reference wind turbines used for simulation are three-bladed downwind HAWT (NREL Phase II and III) rotors, both having the blade sections of the geometric profile of the S809 aerofoil, that were tested comprehensively by the National Renewable Energy Laboratory, Golden, CO, USA [19,28]. Table 1 and Fig. 1 show the basic machine parameters and rotor geometry of the NREL Phase II and III rotors. More details about the geometry of the wind turbine can be found in Refs. [19,28]. For NREL Phase II, the surface pressure distributions were measured at 30%, 47%, 63%, and 80% of the rotor radius using 28 taps per station, while for NREL Phase III, these were measured at five spanwise locations: 30%, 47%, 63%, 80%, and 95% span using 22 pressure taps. The surface pressure sensors were then integrated to obtain the aerodynamic loads at these spanwise locations.

During the NREL Phase II measurements, the inflow conditions were measured at three locations in the upwind direction of the rotor: the north met tower, the local met tower, and the vertical plane array (VPA). Local inflow measurements were installed 2D ($12\,m$) upwind of the turbine on the VPA as presented in Fig. 1. This array contains eight prop-vane anemometers arranged in a circle (spaced in 45° increments) corresponding to 80% of the blade span

Table 1
Basic machine parameters and rotor geometry of the NREL Phase II and III rotors.

	Phase II	Phase III
Number of Blades	3	3
Rotor diameter	10.1 *m*	10.046 *m*
Hub height	17.03 *m*	17.03 *m*
Type of rotor	fixed	fixed
Rotational speed	71.63 rpm synchronous speed	71.63 rpm synchronous speed
Rated power	19.8 kW	19.8 kW
Tilt	0°	0°
Cone angle	3.417°	3.417°
Rotor overhang	1.32 *m*	1.32 *m*
Power regulation	stall	stall
Blade pitch angle	12°	3°
Blade profile	NREL S809	NREL S809
Blade chord	0.4572 *m* at all span stations	0.4572 *m* at all span stations
Blade twist	untwisted	highly twisted

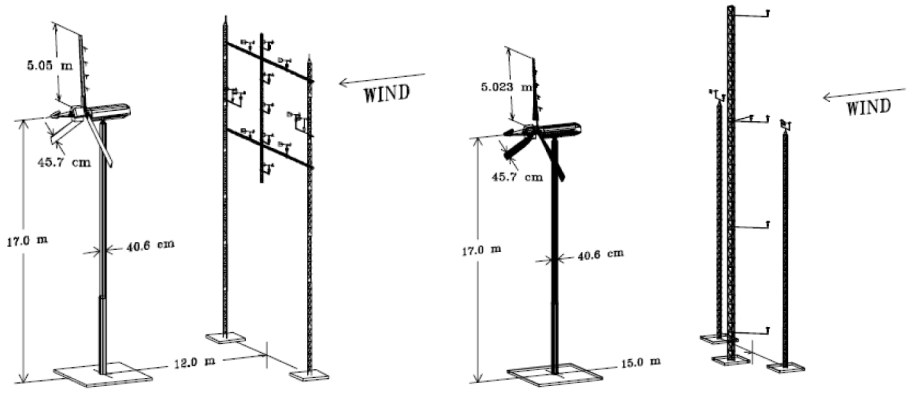

(a) NREL Phase II (b) NREL Phase III

Fig. 1. NREL Phase II and Phase III test configurations [19,28].

with a center prop-vane anemometer installed at the hub height. The array also contains four prop-vane anemometers on an inner circle corresponding to 40% of the blade span. During the NREL Phase III, inflow conditions were also measured directly but using three met towers (see Fig. 1) located 1.5D (15 *m*) upwind of the turbine supported multiple cup anemometers, bi-vane anemometers and one sonic anemometer.

Because the available measured wind speeds are limited between minimum of around 7 m/s to approximately 13 m/s, the highest wind speed test cases were selected from measurements of each wind turbine for validations as illustrated in Table 2. These data have been selected because it is expected that these data encounter stall delay, dynamic stall phenomena and significant cycle-to-cycle variations in various aerodynamic parameters.

3. The classical blade element momentum theory

The BEM method has been widely used for wind turbine applications and for the evolution of wind turbine rotor blade aerodynamic performance. This method is a combination of blade-element theory and momentum theory [29]. Indeed, in the classical BEM model, the aerodynamic loads on a rotating blade are estimated by lookup tables obtained from tests conducted on aerofoils characteristics in a 2D wind tunnel. However, the direct applications of the 2D aerofoil for wind turbines showed significant disagreements between measurements and predictions. The limitations of the BEM theory are well known. These primarily originate from the lack the physics for modelling the complex three-dimensional flow fields that lead to stall-delay and dynamic stall phenomenon to be experienced by the rotating wind turbine blades. The summary of the classical BEM algorithm based on the AeroDyn [29] implementation is shown in Fig. 2.

4. Overview of the models implemented in the modified bem model

There are various corrections that are performed to improve the accuracy of the classical BEM theory [31–34], including the most recent advances in deriving a robust solution algorithm for BEM theory as implemented in QBladed [35] and FAST [36] codes. Although the latter models cater for the complex influence of the three-dimensional flow fields, they are still based on a fixed point

Table 2
The considered test cases of the downwind baseline configuration of the NREL measurements.

Test case	Mean wind speed (*m/s*)	Standard deviation (*m/s*)	Pitch angle (*deg*)	Yaw angle (*deg*)
NREL Phase II	13.1	1.137	11.4	22.8
NREL Phase III	12.8	1.246	3.7	20.7

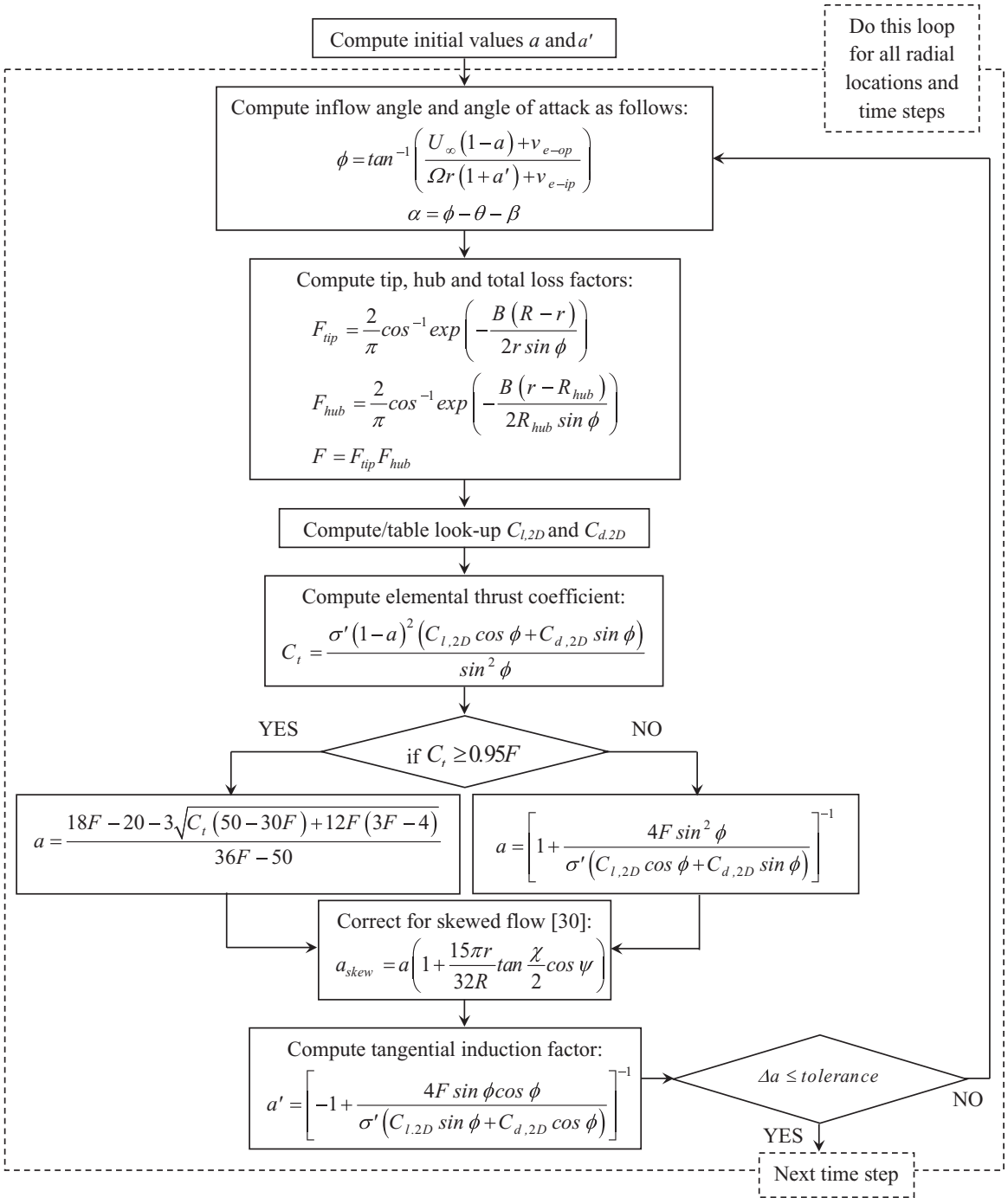

Fig. 2. Diagram for determination of induction factors and aerodynamic forces using iterative process [30].

spectrum model for simulation of the stochastic wind speed creating a weakness in the base code for modelling wind turbines in open field operating conditions. To further improve the accuracy of the classical BEM model, the influence of wind fluctuations on a rotating blade and various unsteady models are implemented in the classical BEM model to cater for the complex influence of the three-dimensional flow fields more reliably, particularly in open field operating conditions where an unsteady inflow is present. These models are being reviewed as follows:

4.1. Stall delay model

In the BEM model, the 2D aerofoil lift and drag force coefficients are corrected for stall delay using the New Stall Delay Model (NSDM) developed by Elgammi and Sant [37]. This model uses a new strategy for correcting the 2D aerofoil characteristics for stall delay to improve aerodynamic load predictions at large angles of attack and extending the applicability of the stall delay correction to yawed rotor conditions. Summary of this model is presented in Fig. 3.

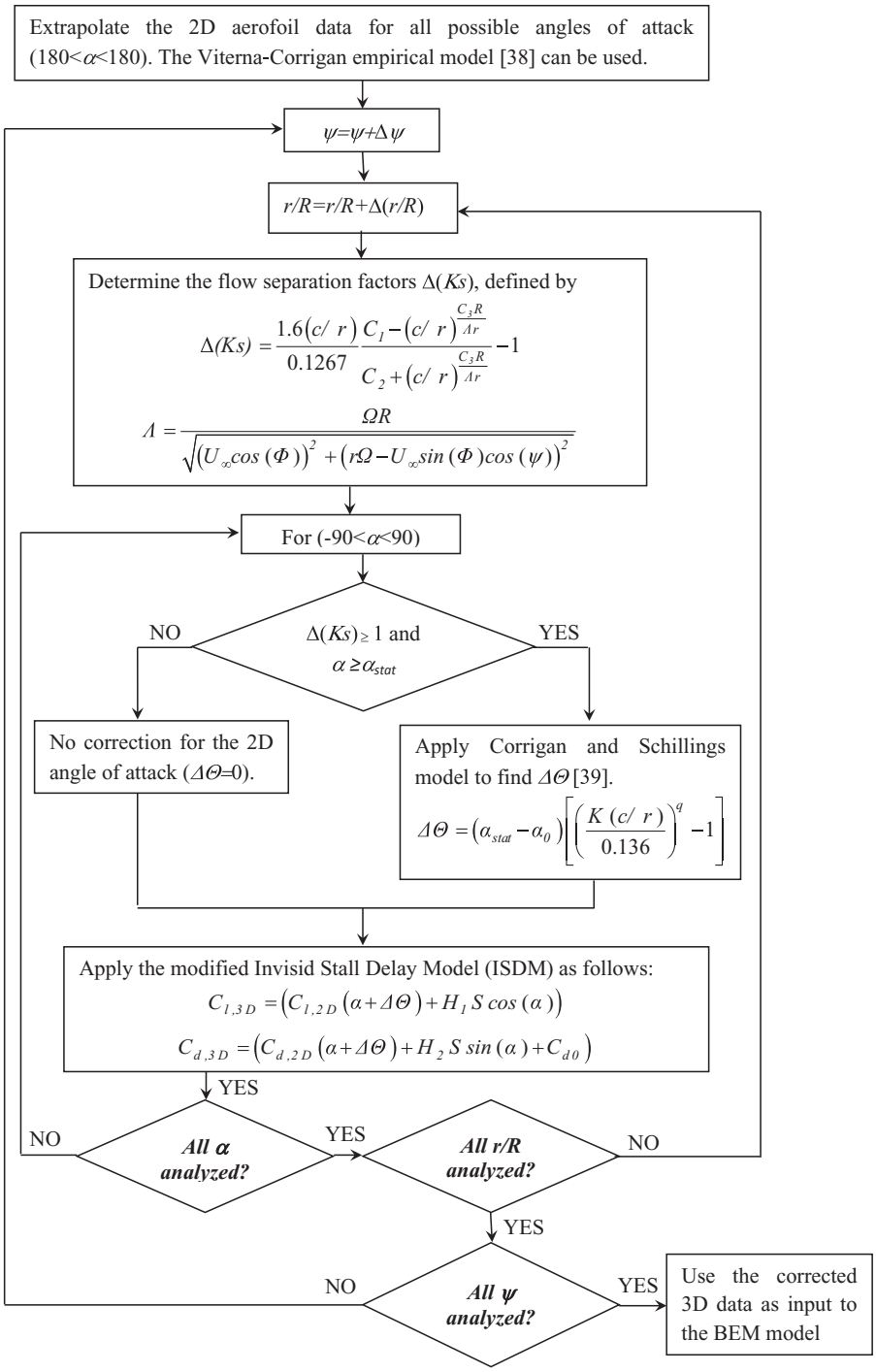

Fig. 3. Schematic process of the new stall delay (NSDM) model [38,39].

4.2. Turbulence model

The method used to generate a file of turbulent wind time series for the BEM code of the present study is the Pacific Northwest Laboratories (PNL) simulation theory which was developed by Powell and Connell [26]. This approach is mainly based on an autocorrelation function for wind on a single rotating point given as follows:

$$P(\tau) = 2/\Gamma(1/3)\left(b_1{}^2 \sin^2(\tau) + b_2{}^2\tau^2\right)^{1/6}(D-E) \quad (1)$$

$$D = K_{1/3}\left[2\left(\beta_1{}^2 \sin^2(\tau) + \beta_2{}^2\tau^2\right)^{1/2}\right]$$

$$E = \frac{\beta_1{}^2 \sin^2(\tau)}{\left(\beta_1{}^2 \sin^2(\tau) + \beta_2{}^2\tau^2\right)^{1/2}} K_{2/3}\left[2\left(\beta_1{}^2 \sin^2(\tau) + \beta_2{}^2\tau^2\right)^{1/2}\right]$$

Γ is the gamma function, $K_{1/3}$ and $K_{2/3}$ are modified Bessel function of fractional order 1/3 and 2/3 respectively, τ is dimensionless time variable in terms of the dimensionless parameters β_1 and β_2.

Harmonics are next randomly selected by Gaussian white noise, while a turbulence time series at one point of a rotating blade is created by an inverse Fourier transform to the correlation function into a power spectrum as:

$$S_p(N) = 4\sigma^2 \int_0^\infty P(\tau)\cos(2\pi N\tau)d\tau \tag{2}$$

Eqn (2) is further transformed to a spectrum of dimensional frequency n using:

$$S_p(n) = 2S_p(N)/\Omega \tag{3}$$

where σ is the standard deviation of the wind speed, N is dimensionless frequency and Ω is the angular velocity.

The change in the mean wind velocity distribution due to the atmospheric boundary layer with different heights above the ground is described by:

$$\overline{U}_\infty(z_2) = \overline{U}_\infty(z_1)\ln(z_2/z_0)/\ln(z_1/z_0) \tag{4}$$

where z_0 is the surface roughness length, z_2 is the height above the ground, z_1 is the reference height, and $\overline{U}_\infty(z_1)$ is the reference velocity at the height z_1.

The process has been implemented in MATLAB© to produce a rotational time series of velocities normal to the whole rotor disc. However, it should be noted that the PNL simulation theory creates a rotational time series for one point at a time. Therefore, the code was used to generate two rotational time series of velocities at each individual blade azimuth angle: one at the turbine hub and the other at the blade tip. Linear interpolation was then applied to obtain wind velocity inputs for intermediate blade radial locations as required by the discretization scheme adopted in the BEM model over a number of rotor rotations (cycles). In this step, it is assumed that the PNL simulation theory provides good correlation for different individual radial locations using the same starting seed. This will be proved to be adequate when the predicted load responses along the blade are compared to measurements.

4.3. Tower shadow model

The tower shadow is a region where reduced wind speed and high turbulence are presented. In this region the blade of the wind turbine passes once per revolution. For downwind mounted rotors, the tower wake can be modelled as a velocity deficit as presented by Wang et al. [40] in the form of a cosine function as follows:

$$\frac{U}{U_\infty} = 1 - \frac{D_v}{2}\left(1 + \cos\left(2\pi\left(\psi_t - \frac{\pi}{2}\right)\Big/2\psi_o\right)\right) \tag{5}$$

where U is the velocity within tower shadow, D_v is the maximum velocity deficit, and U_∞ is the free stream velocity which is divided into two components: a mean wind speed part $\overline{U}_\infty$ and a turbulent fluctuation part u' such as $(U_\infty = \overline{U}_\infty + u')$. The angles ψ_o and ψ_t are defined by:

$$\psi_o = \tan^{-1}\left(\frac{B_t}{2r\sin\psi_1}\right) \tag{6}$$

$$\psi_t = \frac{\pi}{2} - \tan^{-1}\left(\frac{r\cos\Phi\cos\psi - z_t\sin\Phi}{r\sin\psi_1}\right) \tag{7}$$

For yawed flow conditions, the tower shadow region is not centered at around 180° azimuth angle like in axial flow conditions. Therefore, it is vital to account for the skewed tower wake. This is achieved by the use of the azimuthal angles ψ_1 and ψ_2 through which the blade enters and leaves the region of tower shadow. These angles also vary with the blade spanwise location r and can be calculated as follows [40]:

$$\psi_1 = \cos^{-1}\left(\frac{z_t\sin\Phi + 0.5B_t}{r\cos\Phi}\right) \tag{8}$$

$$\psi_2 = \cos^{-1}\left(\frac{z_t\sin\Phi - 0.5B_t}{r\cos\Phi}\right) \tag{9}$$

where z_t is the distance from the yawing axis to the rotor rotation plane, Φ is the yaw angle, and B_t is the tower shadow width.

It was shown by Snyder and Wentz [41] that the tower shadow width and maximum value of velocity deficit generally depend on the streamwise distance downstream, Reynolds number, and the boundary-layer separation (laminar or turbulent). Variations of these parameters were observed from wind tunnel tests for Reynolds numbers from 1.74×10^5 to 7.58×10^5 and it was found that the maximum velocity deficit, at three cylinder diameters downstream of the cylinder centerline, varies with from around 10% to approximately 30% of the free-stream. Indeed, the corresponding tower shadow width at the higher Reynolds numbers is about 2.5 times the tower diameter. Therefore, the parameters ($D_v = 0.3U_\infty$ and $B_t = 2.5D$) are selected for all analysis and comparisons presented in the results and discussion section.

4.4. Dynamic stall model

The Beddoes–Leishman (B–L) model [42,43] used in the present work with the BEM model, is a semi-empirical model that depends on constants deduced from wind-tunnel measurements. The proper representation of the corrected 3D aerodynamic data for stall delay by the NSDM [37] is further corrected by the B–L model to represent the unsteady aerodynamic lift and drag force coefficients. In the B–L model, three physical phenomena are modelled through separate modules: (i) attached flow module, (ii) separated flow module and (iii) vortex-induced flow module. These are coupled in an open loop to correct the lift and drag force coefficients obtained from the BEM model at each time step and for all radial locations on the whole rotor disc. However, the following notes need to be carefully considered to cater for the unsteady behaviour of the tower shadow and also the combined influence of both stall delay and dynamic stall kinematics on a rotating blade:

1. To implement the unsteady tower shadow response when the blade passes through the tower shadow of the wind turbine, the new tower shadow model proposed by Leishman [20] is used. The latter model is based on the Küssner function used for simulating the response of the blade during its passage through tower shadow. Details of these models can be found in Refs. [20,42].
2. The aerodynamic parameters like the first and second critical normal force coefficients, some dependent constants on the 2D aerofoil static data and the flow separation points in the B–L model [42,43] should be all evaluated from the 3D corrected aerofoil data for rotational augmentation, not from the 2D aerofoil static data.

5. The modified blade element momentum model

The proposed modifications to the classical BEM model in this paper are summarized as follows:

1. The input 2D aerofoil static data are corrected for rotational augmentation using the new stall delay (NSDM) model [37] presented in Fig. 3.
2. The instantaneous wind field and tower shadow influences are considered in the calculations using the turbulence model (Eqns. (1)–(4)) and the tower shadow model (Eqns. (5)–(9)) respectively.
3. One of the most important parameter in predicting the unsteady aerodynamic loads on a rotating blade is the angle of attack. Lack of its prediction will lead to disagreement with measurements, especially in uncontrolled flow conditions due to the significant impacts of the unsteady shed vorticity and the effects of the skewed wake. Therefore, the angle of attack (α) in the proposed BEM algorithm is determined by:

$$\alpha = \tan^{-1}\left(\frac{V_y(1-a)}{V_x(1+a')}\right) \tag{10}$$

where V_x and V_y are the x and y components of the velocity along the blade quarter-chord (lifting-line) in the blade coordinate system. In the modified BEM model, these components cater for the effects of shear, turbulent, tower shadow, blade motion, and blade orientation (with respect to the yaw, tilt, cone, pitch, twist, and blade azimuth angles).

4. The other formulas presented in the iterative producer in Fig. 2 are used except the evaluation of the aerodynamic loads from the 2D lookup aerofoil static data. At this step, the 3D lift and drag force coefficients obtained from the new stall delay (NSDM) model (Fig. 3) are further corrected for dynamic stall influence using the B–L model explained in Subsection 4.4.

6. Results and discussion

To validate the proposed BEM algorithm, it is first required to validate the input turbulent wind speed time series described in Subsection 4.2. Powell and Connell [26] provided the measured wind speeds arranged in a circle of anemometers in a vertical plane array and subsequently, the rotational spectra was obtained and theoretically modelled given that a rotating wind turbine blade experiences different turbulence characteristic than that on a stationary point. The PNL simulation theory (see Subsection 4.2) was used in this paper because (1) the frequency content of the simulated loads can be provided at harmonics of the rotor speed relatively well, (2) the method is applicable for small and large rotors, (3) the method can provide reasonable results compared to measurements by analyzing data of only one anemometer to determine input values such as mean wind speed, standard deviation, and integral length scale, and (4) the simulation procedure is fast.

Fig. 4 shows logarithmic plots for the theoretical spectrum created by Fourier transformation of an autocorrelation function of von Karman [44], the simulated theoretically rotational spectra (PNL theory), and the rotational spectra of the experimental data at different radial locations of the blade where the wind speed measurements are available for comparisons. In these plots, it can be seen that the PNL theory slightly under/over-predicts the measured values. However, the estimations are still quite good given that the differences could be mainly related to the noise in the measurements. As recommended by George [45], the measurements at each anemometer should be subjected to low-pass filtering before doing the rotational sampling, but this was not applied in this paper. Indeed, the differences between the PNL theory/measured rotational and von Karman predictions are due to the fact that the spectrum at a rotating point is not the same as that at a fixed point due to the rotational effect. Therefore, it may be noted that a rotational spectrum contains a substantial shift of the frequency content to the frequency of rotation which are not presented in the results of von Karman theory. This was also observed in the simulation results of wind speed turbulence in large wind turbines [25]. For this reason, it was found that it is suitable to simulate the wind speed fluctuations by the PNL theory in this paper.

In all the comparisons presented in this section, the discretization scheme adopted in the BEM model is made with 31 radial elements and 10° blade azimuth angle step. The comparisons have been also conducted for 18 rotor rotations (cycles). The total central processing unit (CUP) times spent on the full simulation of the turbulence-induced blade loads are 17 min for the NREL Phase II rotor and 18 min for the NREL Phase III rotor. Table 3 illustrates the input values to the PNL simulation theory: the mean wind speed, standard deviation, longitudinal and lateral integral scales, and turbulence intensity for the test cases shown in Table 2. The latter input parameters were calculated by curve fitting the Von Karman Spectrum formula to hub-height anemometer data.

Fig. 5 depicts the average of the unsteady angle of attack distributions over 18 rotor rotations at different radial locations as a function of the blade azimuth angle for the NREL Phase II and III rotor test cases (Table 2). These results are estimated by the proposed BEM model (with the PNL model). In fact, angles of attack on a rotating cannot be measured because of that the flow passing by the blade is influenced by the complex flow field in the near wake. Therefore, no comparisons with measurements were done in Fig. 5.

Figs. 6 and 7 present comparisons of the normal force and tangential force coefficients between the proposed BEM model (with von Karman model), proposed BEM model (with PNL model), classical BEM model and the field data at three spanwise blade locations for the test cases presented in Table 2. These figures are presented as the average values of the normal and tangential force coefficients because comparisons of the full set of 18 rotor rotations with measurements in one plot will not give a clear indication on comparisons of each individual cycle. Instead, the maximum and minimum normalized standard deviations were determined at each radial location and organized in Tables 4 and 5. It can be seen from these comparisons that the normal force coefficient C_N and tangential force coefficient C_T determined using the proposed BEM model (with PNL model) compare well with the experiment at most of the blade sections although some deviations from measurements are still seen, particularly at the inboard sections. These comparison show that predictions of the proposed BEM model (with PNL model) are better than those obtained from the proposed BEM model (with von Karman model) which reflect the fact that a rotating wind turbine blade experiences different turbulence characteristic than that on a stationary point such that determined by von Karman model.

Predictions of the cycle-to-cycle variations using the proposed BEM model (with PNL model) (see the maximum and minimum normalized standard deviations given in Tables 4 and 5) are in good agreements with measurements, but not perfect especially in the stall flow regime and in the region of tower shadow, where higher unsteady fluctuations in the unsteady aerodynamic loads are usually seen. In fact, perfect predictions of these cyclic aerodynamic loads are impossible due to the net effect on the wind turbine rotors under an adverse, unsteady aerodynamic environment which is difficult to define using measurements and to predict using mathematical models [20]. Overall, it could be observed that the

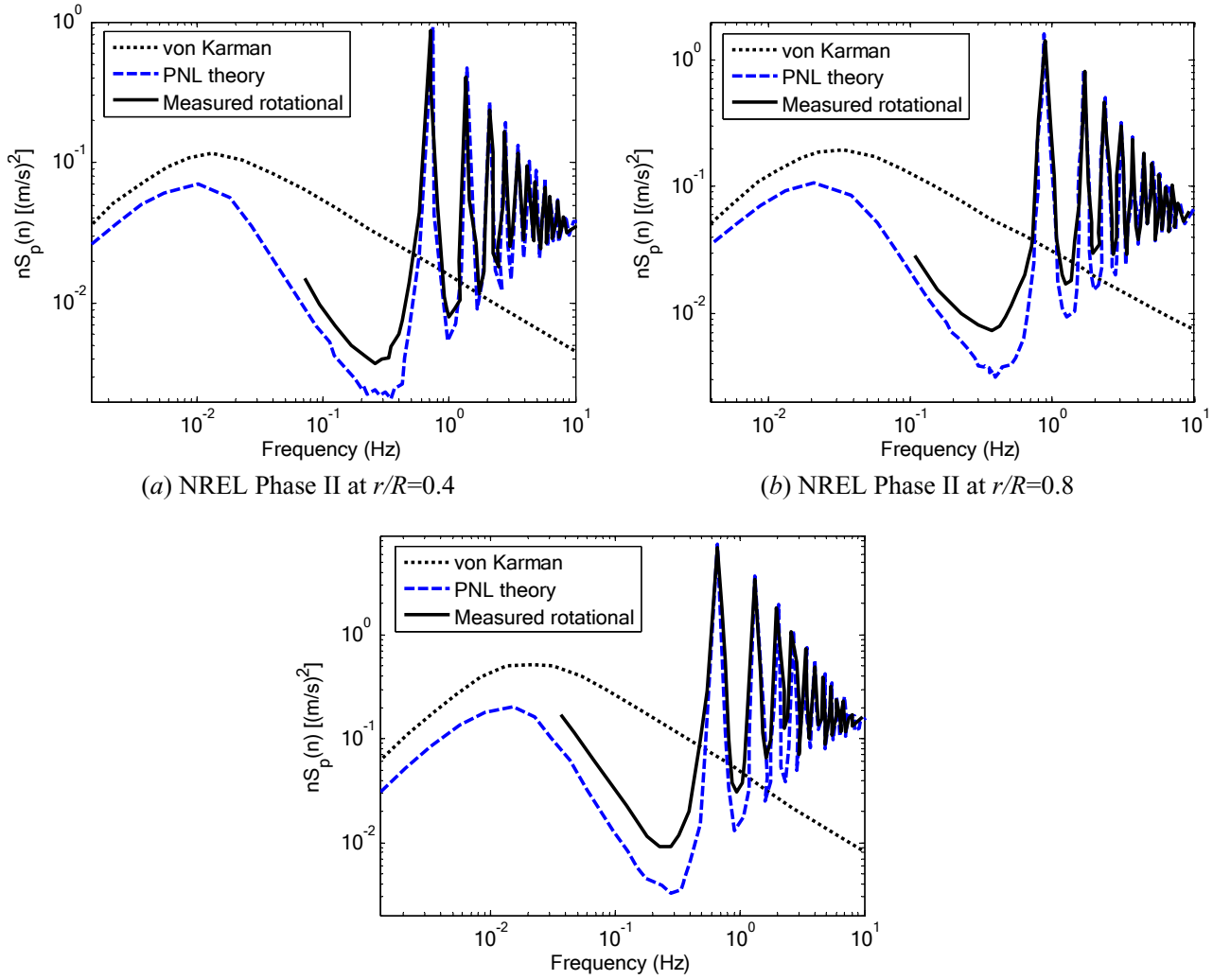

(*a*) NREL Phase II at *r/R*=0.4

(*b*) NREL Phase II at *r/R*=0.8

(*c*) NREL Phase III at *r/R*=1

Fig. 4. Comparisons between the von Karman, PNL theory and rotational spectra of the experimental data.

Table 3
Input parameters to the PNL simulation theory.

Parameters	Test case	
	NREL Phase II	NREL Phase III
Mean wind speed (m/s)	13.1	12.8
Standard deviation (m/s)	1.137	1.246
Longitudinal integral scale (m)	42	38
Lateral integral scale (m)	17	15
Turbulence intensity (−)	0.0868	0.0973

highly twisted blade (NREL Phase III) experiences higher cycle-to-cycle variations in the aerodynamic parameters than that on the untwisted blade (NREL II) (see Tables 3 and 4) except at the blade tip, where it seems that the latter encounters higher pressure gradients leading to higher circulation and swirl velocities than that on the tip of the twisted blade tip. Indeed, high level of uncleanness in the flow regime over the blade aerofoil sections leads to unsteady dynamic stall vortex and high cycle-to-cycle variation in the aerodynamic loads (high standard deviations) when the static stall angle of the aerofoil (15.3°) is exceeded (see Fig. 5).

From Fig. 6 (NREL Phase II test case given in Table 2), it was found that the mean angle of attack distribution decreases from 30.7° at $r/R = 0.30$, down to below 14° at $r/R = 0.63$ and 8.4 at $r/R = 0.8$ (see Fig. 5 (a)). The corresponding maximum angles of attack to these blades sections are 38.9°, 20.7°, and 12.8° respectively which highly exceed the S809 aerofoil static stall angle of 15.3° [19], particularly at the middle and inboard sections of the blade. Therefore, it is expected that the effects of 3D stall delay and dynamic stall phenomena are significant for this test case (see the normalized standard deviations for the NREL Phase II in Table 4). On the other hand, it should be observed that the high fluctuations in the unsteady aerodynamic loads along the blade come from not only due to the consequences of the dynamic stall kinematics but also from the fluctuation in the turbulent wind speed, which impacts on the variation of angle of attack (see Fig. 5 (a)) and relative velocity along the blade. Although the maximum angle of attack at $r/R = 0.80$ is still below the static stall angle of 15.3°, one can also observe that this blade section experiences significant fluctuation which may show the unsteady influences of turbulent wind speed and tower shadow in the attached flow regimes and at low angles of attack. Estimations of the aerodynamic loads including the cycle-to-cycle variations due to turbulent wind speed are generally good indicating the capability of the proposed BEM model (with PNL model) to accurately estimate the blade aerodynamic loads in

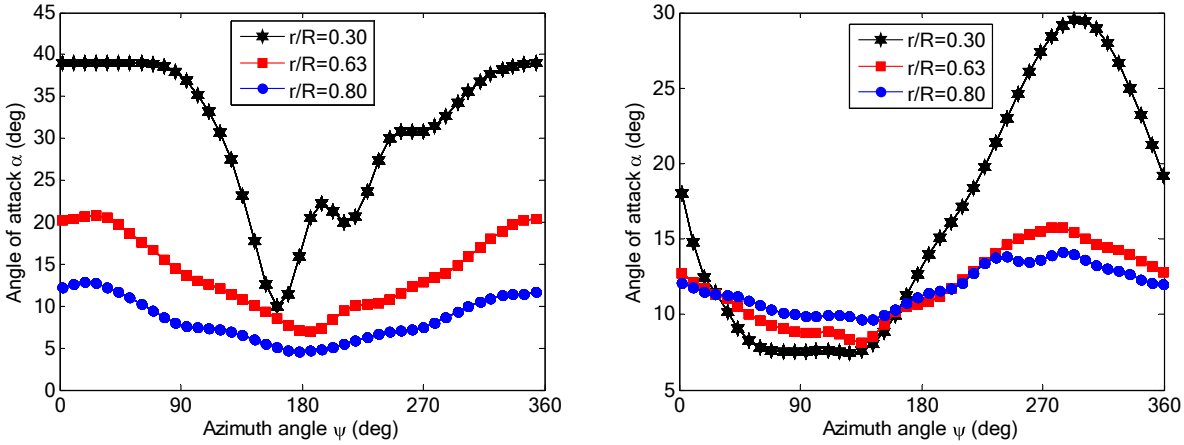

(*a*) NREL Phase II rotor (*b*) NREL Phase III rotor

Fig. 5. Average of unsteady angle of attack against the blade azimuth angle (NREL Phase II and III rotors).

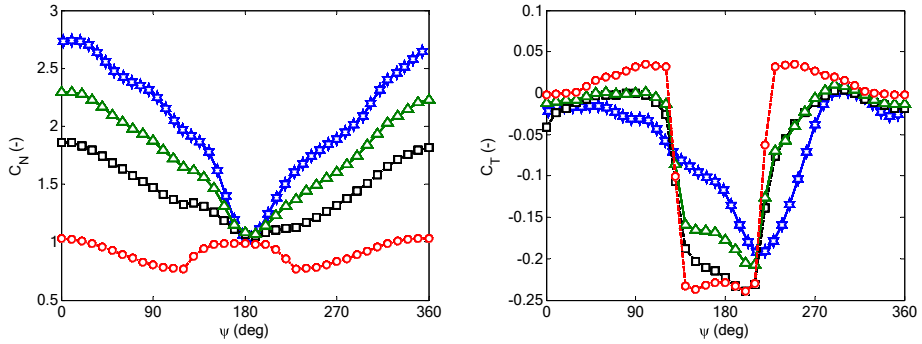

(*a*) C_N and C_T at r/R=0.30

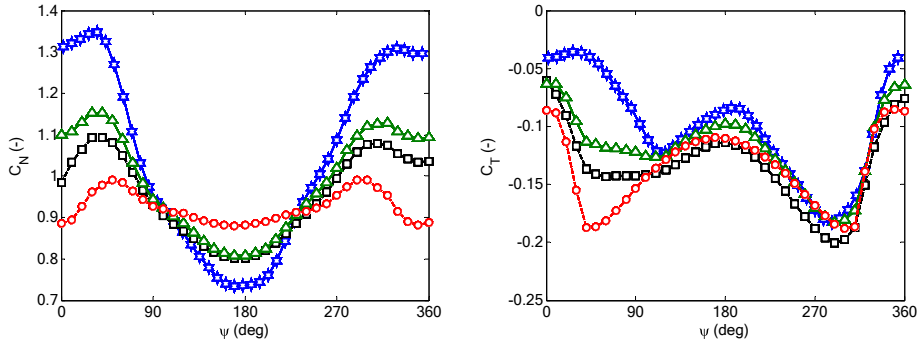

(*b*) C_N and C_T at r/R=0.63

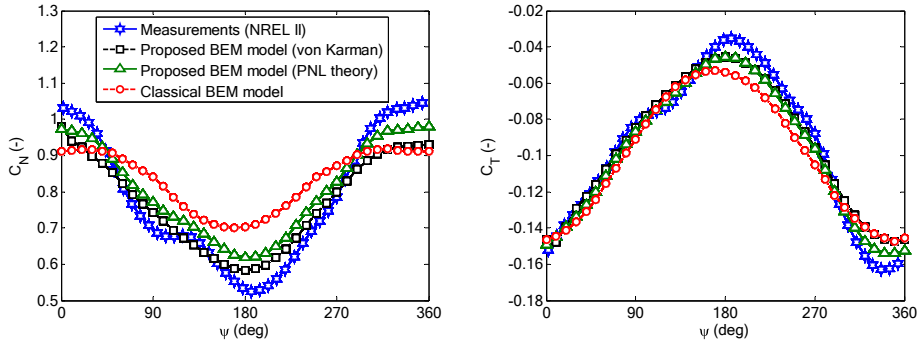

(*c*) C_N and C_T at r/R=0.80

Fig. 6. Comparisons of the unsteady normal and tangential force coefficients predicted by the classical and proposed BEM models with measurements at different radial locations (NREL Phase II rotor).

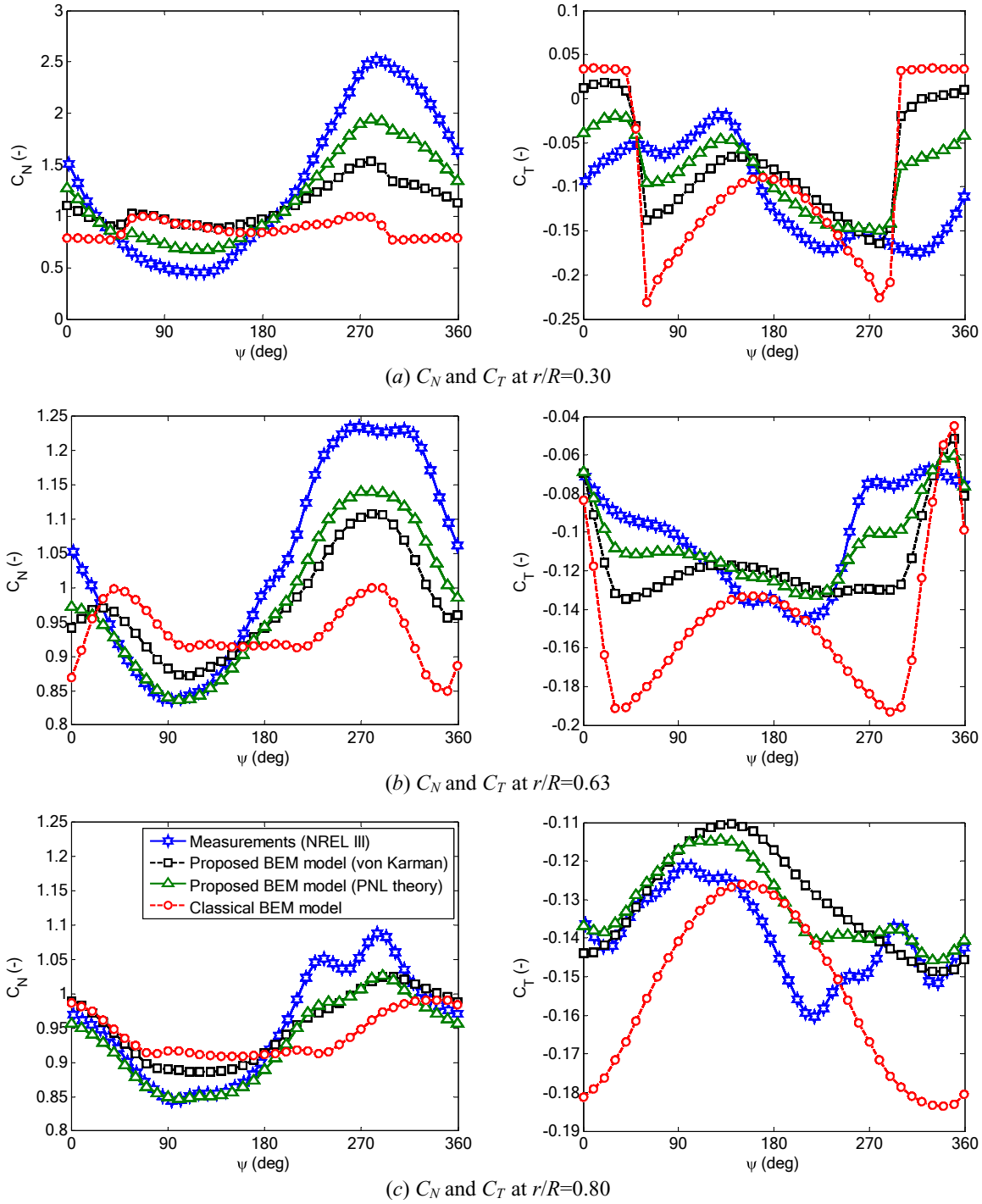

(*a*) C_N and C_T at r/R=0.30

(*b*) C_N and C_T at r/R=0.63

(*c*) C_N and C_T at r/R=0.80

Fig. 7. Comparisons of the unsteady normal and tangential force coefficients predicted by the classical and proposed BEM models with measurements at different radial locations (NREL Phase III rotor).

yawed flows for high angles of attack.

In Fig. 7 (NREL Phase III test case shown in Table 2), the average angle of attack at $r/R = 0.30$ was found to be around 16.3° and reduces to approximately 11.8° at $r/R = 0.63$ to 11.7° at $r/R = 0.80$ (see Fig. 5 (b)). For this test case, the maximum values of the predicted angles of attack are 30.6° at $r/R = 0.3$, 15.7° at $r/R = 0.63$, and 14.1° at $r/R = 0.80$. It is obvious that the maximum angle of attack at the inboard sections of the blade highly exceeds the static stall angle (15.3°) of the S809 aerofoil, while those at the middle and outboard sections are moderate. Therefore these sections may experience attached and separated flows within the same revolution and hence moderate and strong 3D effects along the blades. It seems that the NREL Phase III rotor also has significant cyclic variations in both the unsteady angle of attack (see Fig. 5 (b)) and the aerodynamic load distributions (see the normalized standard deviations for the NREL Phase III in Table 5) which explain the contribution of the stochastic wind speed to the cyclic variations of various aerodynamic parameters. There are some over/under

Table 4
The predicted and measured maximum and minimum normalized standard deviations in the normal and tangential force coefficients on the blades of the NREL II rotor.

Maximum and minimum normalized standard deviation (σ_{CN}/μ_{CN})						
	BEM + von Karman		BEM + PNL		Measurements	
Radial location	Min.	Max.	Min.	Max.	Min.	Max.
r/R = 0.30	0.18	0.35	0.14	0.34	0.11	0.46
r/R = 0.63	0.08	0.15	0.07	0.19	0.06	0.22
r/R = 0.80	0.06	0.22	0.09	0.24	0.08	0.27
Maximum and minimum normalized standard deviation (σ_{CT}/μ_{CT})						
	BEM + von Karman		BEM + PNL		Measurements	
Radial location	Min.	Max.	Min.	Max.	Min.	Max.
r/R = 0.30	0.15	1.86	0.26	2.28	0.24	2.02
r/R = 0.63	0.11	2.51	0.16	2.38	0.20	2.27
r/R = 0.80	0.18	0.68	0.20	0.71	0.23	0.82

Table 5
The predicted and measured maximum and minimum normalized standard deviations in the normal and tangential force coefficients on the blades of the NREL III rotor.

Maximum and minimum normalized standard deviation (σ_{CN}/μ_{CN})						
	BEM + von Karman		BEM + PNL		Measurements	
Radial location	Min.	Max.	Min.	Max.	Min.	Max.
r/R = 0.30	0.28	0.50	0.25	0.91	0.21	1.06
r/R = 0.63	0.04	0.10	0.10	0.22	0.09	0.23
r/R = 0.80	0.02	0.07	0.07	0.14	0.05	0.15
Maximum and minimum normalized standard deviation (σ_{CT}/μ_{CT})						
	BEM + von Karman		BEM + PNL		Measurements	
Radial location	Min.	Max.	Min.	Max.	Min.	Min.
r/R = 0.30	0.11	0.68	0.36	2.10	0.25	1.90
r/R = 0.63	0.24	0.74	0.28	1.10	0.32	1.38
r/R = 0.80	0.14	0.39	0.15	0.42	0.16	0.56

predictions in the unsteady aerodynamic loads as seen from Fig. 7. However, the unsteady the proposed BEM model (with PNL model) predicts the general features of the dynamic stall kinematics and the stall delay phenomena and the cyclic variations of the unsteady normal and tangential force coefficients under uncontrolled conditions fairly good for low, moderate and high angles of attack and in the separated flow regimes.

7. Conclusion

This paper presents a numerical approach in which a BEM model and the Pacific Northwest Laboratories (PNL) Simulation theory are used to simulate the cycle-to-cycle aerodynamic loads response to turbulence over successive rotor rotations for yawed flow conditions in the free stream environment. These methods were integrated to analyze two three-bladed downwind horizontal axis wind turbine rotors developed by the National Renewable Energy Laboratory (NREL). In the PNL simulation theory, the measured wind speed data from an array of nine anemometers located upwind of the turbine were used. The anemometer installed at the turbine hub was used to determine the inputs mean wind speed, standard deviation, and integral length scale. The proposed BEM model (with PNL model) takes into account also the influence of dynamic stall (using Beddoes–Leishman (B–L) model) and the rotational augmentation (using the New Stall Delay Model (NSDM)). The unsteady influence of the tower shadow has been carefully considered under yawed flow conditions. From this study, a number of conclusions and recommendations were made as follows:

- Comparisons of the von Karman fixed point spectrum and PNL rotationally sampled spectrum models showed that the latter is more representative of the stochastic wind speed. This is obvious from the influence of the estimated stochastic wind speed on the predicted aerodynamic loads giving evidence that a rotating wind turbine blade encounters different turbulence characteristic than that on a stationary point due to the rotational effect.
- It was shown that the highly twisted blade (NREL III rotor) has higher cycle-to-cycle variations in the normal and tangential force coefficients than the untwisted blade (NREL II rotor). However, the latter has higher cyclic variations at the blade tip indicating that it encounters higher pressure gradients, circulations and swirl velocities. This is important for design purpose to design a better blade with suitable chord and twist/untwisted sections that are subjected to low cycle-to-cycle variations in the aerodynamic loads.
- The proposed BEM model with the simulated theoretically rotational spectra (PNL model) is able to capture the cycle-to-cycle differences in the unsteady normal and tangential force coefficients, resulting from the complex 3D effects, from one rotor rotation to the next, but not perfectly. It was shown from the comparisons with measurements that significant cycle-to-cycle variations in the aerodynamic loads are not only due to the unsteady kinematics of dynamic stall but also due to the contribution of the turbulent wind speed.
- Generally, the proposed BEM model (with PNL model) shows acceptable results. However, it may also be required to further investigate its validity for different rotor sizes, different turbulent wind speeds and different hub configurations. The developed BEM model could be considered as an important step for predicting turbulence loads of advanced machine designs given that it is fast and relatively accurate compared with CFD and FWVM methods which are more complex and computational

costly methods. Further work will extend the present analysis to larger wind turbine rotors that are more representative of those presently available on the market.

Acknowledgements

The authors would like to thank the National Renewable Energy Laboratory and Prof. Dr. Schepers J.G., for providing the experimental data of the National Renewable Energy Laboratory.

Nomenclature

a, a'	axial and tangential induction factors, **[−]**
a_{skew}	axial induction factor with correction for skewed flow, **[−]**
b_1	dimensionless parameter (r/L_y), **[−]**
b_2	dimensionless parameter ($U_\infty/\Omega L_x$), **[−]**
B	blade number, **[−]**
B_t	tower shadow width, [m]
c	aerofoil chord, [m]
C_1−C_3	constants of the separation model of Du and Selig, [−]
C_{d0}	zero-lift drag coefficient, [−]
$C_{d,2D}$	drag coefficient for 2D flows, [−]
$C_{d,3D}$	drag coefficient corrected for 3D effects (stall delay), [−]
$C_{l,2D}$	lift coefficient for 2D flow**s,** [−]
$C_{l,3D}$	lift coefficient corrected for 3D effects (stall delay), [−]
C_N	normal force coefficient, [−]
C_t	thrust coefficient, [−]
C_T	tangential force coefficient, [−]
D_v	maximum velocity deficit, [m/s]
F	total loss factor, [−]
F_{hub}	hub loss factor, [−]
F_{tip}	tip loss factor, [−]
H_1, H_2	constants equal to 0.5, [−]
n	dimensional frequency ($\Omega N/2$), [rad/s]
N	dimensionless frequency, [−]
K	velocity gradient, [m/s]
$K_{1/3}$	modified Bessel function of fractional order 1/3, [−]
$K_{2/3}$	modified Bessel function of fractional order 2/3, [−]
Ks	flow separation factor, [−]
L_x	longitudinal integral length scales of turbulence, [m]
L_y	lateral integral length scales of turbulence, [m]
q	constant for Corrigan and Schillings stall delay model, [−]
r	local radial position, [m]
R	tip radius, [m]
R_{hub}	hub radius, [m]
S	inviscid stall delay model correction factor, [−]
u'	turbulent fluctuation part of the free-stream wind speed, [m/s]
U	velocity within tower shadow, [m/s]
U_∞	free-stream wind speed, [m/s]
$\overline{U}_\infty$	mean wind speed, [m/s]
$v_{e\text{-}ip}$	in-plane element velocity due to blade motion, [m/s]
$v_{e\text{-}op}$	out-of-plane element velocity due to blade motion, [m/s]
z_t	distance from the yawing axis to the rotor rotation plane, [m]
α	angle of attack, [deg]
α_0	zero lift angle of attack, [deg]
α_{stat}	static stall angle, [deg]
β	pitch angle, [deg]
β_1	dimensionless parameter (r/L_y), [−]
β_2	dimensionless parameter ($\overline{U}_\infty/\Omega L_x$), [−]
$\Delta\Theta$	stall delay correction for 2D angle of attack, [deg]
θ	twist angle, [deg]
Λ	modified tip speed ratio for the Du and Selig model, [−]
μ_{CN}	mean of normal force coefficient, [−]
μ_{CT}	mean of tangential force coefficient, [−]
σ	standard deviation of the wind speed, [m/s]
σ'	local solidity, [−]
σ_{CN}	standard deviation of normal force coefficient, [−]
σ_{CT}	standard deviation of tangential force coefficient, [−]
τ	dimensionless time variable, [−]
ϕ	inflow angle, [deg]
Φ	yaw angle, [deg]
χ	total wake skew anglem, [deg]
ψ	blade azimuth angle, [deg]
ψ_1,ψ_2	azimuth angles where blade passes through tower shadow region, [deg]
Γ	gamma function. [−]
Ω	rotation speed of rotor, [rad/s]

References

[1] M. Khaled, M.M. Ibrahim, H.E. Abdel Hamed, A.F. Abdel Gawad, Aerodynamic design and blade angle Analysis of a small horizontal−Axis wind turbine, Am. J Mod. Energy 3 (2) (2017) 23−37.
[2] S. Rehman, M.M. Alam, L.M. Alhems, M.M. Rafique, Horizontal Axis wind turbine blade design methodologies for efficiency enhancement—a review, Energies 11 (2018) 506.
[3] J.N. Sørensen, Aerodynamic aspects of wind energy conversion, Annu. Rev. Fluid Mech. 43 (2011) 427−448.
[4] H.M. Lee, Y. Wu, An experimental study of stall delay on the blade of a horizontal-axis wind turbine using tomographic particle image velocimetry, J. Wind Eng. Ind. Aerodyn. 123 (2013) 56−68.
[5] D. Hu, O. Hua, Z. Du, A study on stall-delay for horizontal axis wind turbine, J. Renew. Energy 31 (2006) 821−836.
[6] I. Herráez, B. Akay, G.J.W. van Bussel, J. Peinke, B. Stoevesandt, Detailed analysis of the blade root flow of a horizontal axis wind turbine, Wind Energy Sci. 1 (2) (2016) 89−100.
[7] M. Ramasamy, J.S. Wilson, W.J. McCroskey, P.B. Martin, Measured Characteristics of Cycle-To-Cycle Variations in Dynamic Stall. 2016 AHS Technical Meeting on Aeromechanics Design for Vertical Lift, at San Francisco, CA, Jan. 2016.
[8] K. Mulleners, A.L. Paper, B. Heine, M. Raffel, The dynamics of static stall, in: 16th Symposium on Applications of Laser Techniques to Fluid Mechanics, Lisbob, Portugal, July 2012, 0912.
[9] Q. Li, Y. Kamada, T. Maeda, M. Murata, Y. Nishida, Effect of turbulent inflows on airfoil performance for a Horizontal Axis Wind Turbine at low Reynolds numbers (part I: static pressure measurement), Energy 111 (2016) 701−712.
[10] S. Schreck, The NREL full-scale wind tunnel experiment−introduction to the special issue, Wind Energy 5 (2−3) (2002) 77−84.
[11] D. Simms, S. Schreck, L. Fingeresh, NREL Unsteady Aerodynamics Experiment in the NASA-Ames Wind Tunnel: A Comparison of Predictions to Measurements, National Renewable Energy Laboratory, Golden, CO, USA, 2001. Technical Report NREL/TP-500-29494.
[12] J.G. Schepers, Engineering Models in Wind Energy Aerodynamics: Development, Implementation and Analysis Using Dedicated Aerodynamic Measurements, Ph.D. Thesis, TUDelft, 2012.
[13] C.P. Butterfield, W.P. Musial, G.N. Scott, D.A. Simms, NREL Combined Experiment Final Report-phase II, National Renewable Energy Laboratory, Golden, CO, USA, 1992. NREL/IP-442-4807.
[14] C.P. Butterfield, W.P. Musial, D.A. Simms, Combined Experiment Phase I – Final Report, National Renewable Energy Laboratory, Golden, CO, USA, 1992. NREL/TP-257-4655.
[15] T.L. Acker, M.M. Hand, Aerodynamic Performance of the NREL Unsteady Aerodynamics Experiment (Phase IV) Twisted Rotor, *37th Aerospace Sciences Meeting and Exhibit*, Reno, USA, 11−14 Jan. 1999.
[16] L.J. Fingersh, D.A. Simms, C.P. Butterfield, M.D. Jenks, Overview of the Unsteady Aerodynamics Experiment Phase III Data Acquisition System and Instrumentation vol. 95, ASME Energy and Environment Expo, Houston, TX, Jan.−Feb. 1995.
[17] J.G. Schepers, A.J. Brand, A. Bruining, J.M.R. Graham, M.M. Hand, D.G. Infield, H.A. Madsen, R.J.H. Paynter, D.A. Simms, Final Report of IEA Annex XIV: Field Rotor Aerodynamics, Netherlands Energy Research Foundation ECN, Petten, The Netherlands, May 1997. Technical Report ECN-C-97-027.
[18] J.G. Schepers, A.J. Brand, A. Bruining, J.M.R. Graham, M.M. Hand, D.G. Infield, H.A. Madsen, T. Maeda, J.H. Paynter, R. van Rooij, Y. Shimizu, D.A. Simms, N. Stefanatos, Final Report of IEA AnnexXVIII: Enhanced Field Rotor Aerodynamics Database, Netherlands Energy Research Foundation ECN, Petten, The Netherlands, Feb. 2002. Technical Report ECN-C-02-016.

[19] J.G. Schepers, R.P.J.O.M. van Rooij, Final Report of the Annexlyse Project: Analysis of Aerodynamic Field Measurements on Wind Turbines, Netherlands Energy Research Foundation ECN, Petten, The Netherlands, Jun. 2005. Technical Report ECN-C-05-064.
[20] J.G. Leishman, Challenges in modelling the unsteady aerodynamics of wind turbines, Wind Energy 5 (11) (2002) 85–132.
[21] M. Cormier, M. Caboni, T. Lutz, K. Boorsma, E. Krämer, Numerical analysis of unsteady aerodynamics of floating offshore wind turbines, J. Phys. 1037 (2018), 072048. Conf. Series.
[22] L.J. Vermeer, J.N. Sørensen, A. Crespo, Wind turbine wake aerodynamics, Prog. Aero. Sci. 39 (2003) 467–510.
[23] J.G. Schepers, K. Boorsma, X. Munduate, Final Results from Mexnext-I: analysis of detailed aerodynamic measurements on a 4.5 m diameter rotor placed in the large German Dutch Wind Tunnel DNW, J. Phys. 555 (1) (2014), 012089. Conf. Series.
[24] J. Bartl, L. Sætran, Blind test comparison of the performance and wake flow between two in-line wind turbines exposed to different turbulent inflow conditions, Wind Energy Sci. 2 (1) (2017) 55–76.
[25] A. Burlibaşa, E. Ceangă, Rotationally sampled spectrum approach for simulation of wind speed turbulence in large wind turbines, Appl. Energy 111 (2013) 624–635.
[26] D.C. Powell, J.R. Connell, A Model for Simulating Rotational Data for Wind Turbine Applications, PNL-5857, Pacific Northwest Laboratory, Richland, Washington, April 1986.
[27] M. Elgammi, T. Sant, Combining unsteady blade pressure measurements and a free-wake vortex model to investigate the cycle-to-cycle variations in wind turbine aerodynamic blade loads in yaw, Energies 9 (6) (2016) 460.
[28] D.A. Simms, M.M. Hand, L.J. Fingersh, D.W. Jager, Unsteady Aerodynamics Experiment Phases II–IV Test Configurations and Available Data Campaigns. Tech. Rep. NREL/TP-500-25950, National Renewable Energy Laboratory, Golden, CO, July 1999.
[29] Patrick J. Moriarty, A. Hansen, Craig. AeroDyn Theory Manual. Tech. Rep. NREL/EL-500-36881, National Renewable Energy Laboratory, Golden, CO, December 2005.
[30] D.M. Pitt, D.A. Peters, Theoretical prediction of dynamic-inflow derivatives, Vertica 5 (1) (March 1981).
[31] A. Ning, A simple solution method for the blade element momentum equations with guaranteed convergence, Wind Energy 17 (9) (2014) 1327–1345.
[32] A. Ning, G. Hayman, R. Damiani, J. Jonkman, Development and Validation of a New Blade Element Momentum Skewed-Wake Model within AeroDyn, 33rd ASME Wind Energy Symposium, Kissimmee, FL, Jan. 2015.
[33] F. Mahmuddin, Rotor blade performance analysis with blade element momentum theory, Energy Procedia 105 (2017) 1123–1129.
[34] R. Lanzafame, S. Mauro, M. Messina, HAWT design and performance evaluation: improving the BEM theory mathematical models, Energy Procedia 82 (2015) 172–179.
[35] D. Marten, J. Wendler, QBlade Guidelines, Berlin Technical University, Berlin, 2013.
[36] J. Jonkman, The New Modularization Framework for the Fast Wind Turbine Cae Tool Tool, 51st *AIAA Aerospac*e Sciences Meeting Including the New Horizons Forum and Aerospace Exposition, Dallas, TX, Jan 2013.
[37] M. Elgammi, Sant, A New Stall Delay Algorithm for Predicting the Aerodynamics Loads on Wind Turbine Blades for Axial and Yawed Conditions, Wind Energy, 2017.
[38] L.A. Viterna, R.D. Corrigan, Fixed Pitch Rotor Performance of Large Horizontal Axis Wind Turbines, DOE/NASA Workshop on Large Horizontal Axis Wind Turbines, Cleveland, Ohio, 28–30 July 1981.
[39] J.J. Corrigan, J.J. Schillings, Empirical Model for Stall Delay Due to Rotation, American Helicopter Society Aeromechanics Specialists Conference, San Francisco, California, 1994, pp. 1–16.
[40] T. Wang, F.N. Coton, A high resolution tower shadow model for downwind wind turbines, J. Wind Eng. Ind. Aerodyn. 89 (2001) 873–892.
[41] M.H. Snyder, W.H. Wentz Jr., Dynamics of Wakes Downstream of Wind Turbine Towers, NASA-CP-2185, 1981.
[42] J.G. Leishman, T.S. Beddoes, A semi-empirical model for dynamic stall, J. Am. Helicopter Soc. 34 (1989) 3–17.
[43] M. Elgammi, T. Sant, A modified Beddoes-Leishman model for unsteady aerodynamic blade load computations on wind turbine blades, J. Sol. Energy Eng. 138 (5) (2016), 051009-051009-18.
[44] T. von Karman, Progress in the statistical theory of turbulence, Proc. Natl. Acad. Sci. U.S.A. 34 (11) (1948) 530–539.
[45] R.L. George, Simulation of Winds as Seen by a Rotating Vertical axis Wind Turbine Blade. PNL-4914, Pacific Northwest Laboratory, *Richland*, Washington, 1984.